

# The CLAS12 beamline and its performance

N. Baltzell<sup>a</sup>, V. Burkert<sup>a</sup>, J. Carvajal<sup>f</sup>, N. Dashyan<sup>b</sup>, R. De Vita<sup>c</sup>, L. Elouadrhiri<sup>a</sup>, G. Kharashvili<sup>a</sup>, A. Kim<sup>d</sup>, R. Paremuzyan<sup>e</sup>, B. A. Raue<sup>f</sup>, S. Stepanyan<sup>a</sup>, M. Ungaro<sup>a</sup>, K. Wild<sup>f</sup>

<sup>a</sup>Thomas Jefferson National Accelerator Facility, Newport News, Virginia 23606

<sup>b</sup>Alikhanian National Laboratory, Yerevan, Armenia

<sup>c</sup>Istituto Nazionale di Fisica Nucleare, Genova, Via Dodecaneso 33, 16146 Italy

<sup>d</sup>University of Connecticut, Storrs, CT 06269-3046

<sup>e</sup>University of New Hampshire, Department of Physics, Durham, NH 03824

<sup>f</sup>Florida International University, Miami, FL 33199

---

## Abstract

This paper describes the Hall B beamline and its performance during the first year of data-taking operation using the CLAS12 detector. We review the beamline instrumentation used to measure and monitor the beam. This instrumentation led to excellent beam quality for energies ranging from 2.3 to 10.6 GeV at the design luminosity of  $10^{35} \text{ cm}^{-2}\text{s}^{-1}$ . The instrumentation includes a Møller polarimeter, which can typically measure the beam polarization to an absolute precision of  $\sim 2.5\%$ .

**Keywords:** electron beam, collimator, heavy photon, electromagnetic calorimeter, polarimeter

---

## 1. Introduction

The physics program for CLAS12 in Jefferson Lab's Hall B requires the use of electron beams of various energies and currents that impinge upon on targets ranging from liquid hydrogen to lead. A significant part of the physics program includes running with polarized targets that require a rastered beam on the target. In order to extract experimental observables, accurate measurements of the beam charge and polarization are required. Also, for safe and efficient operation of a large, open acceptance spectrometer, proper shielding and a stable beam with a small lateral size and minimal beam halo are needed.

The Hall-B beamline is designed to satisfy experimental requirements and provide necessary controls and monitoring of the electron beam properties for safe and efficient operation of CLAS12. The key set of parameters required by experiments with CLAS12 is listed in Table 1. The main challenges for the beamline setup are the open acceptance of CLAS12 and the close proximity of various sensitive detectors to the target and beam. Such challenges were successfully overcome in Hall B in the past for CLAS [1] experiments and the Heavy Photon Search (HPS) experiment [2].

A few key modifications to the beamline [3] used during the lower-energy run of the HPS experiment

Parameter	Requirement	Unit
$E$	$\leq 11$	GeV
$\delta p/p$	$< 10^{-4}$	
Current	50 to 500	nA
Current instability	$\sim 10$	%
$\sigma_x, \sigma_y$	$< 300$	$\mu\text{m}$
Position stability	$< 200$	$\mu\text{m}$
Divergence	$< 100$	$\mu\text{rad}$
Beam halo ( $> 5\sigma$ )	$< 10^{-4}$	
Beam polarization	$> 0.85$	

Table 1: Nominal required Hall B beam parameters.

have been introduced in order to establish high-quality physics beams in Hall B and run CLAS12 at the design luminosity of  $10^{35} \text{ cm}^{-2}\text{s}^{-1}$ . Additions to the beamline for high-energy running of CLAS12 include a new intermediate beam dump upstream of the hall, a cryogenic target system, shielding downstream of the target to protect CLAS12 detectors from electromagnetic backgrounds, and the Møller polarimeter for beam polarization measurements.

This paper will discuss the design of the Hall-B beamline for CLAS12, and its performance during the 2018 experimental run. It will review the beamline instrumentation used to measure and monitor beam pa-

40 parameters and to protect CLAS12 detectors against errant  
41 beam motion. As will be demonstrated, excellent qual-  
42 ity and stability of the CEBAF beams, coupled with the  
43 Hall-B beamline protection systems, allowed running  
44 the CLAS12 detector at the design luminosity.

## 45 2. Hall-B Beamline Design

46 As was described in Ref. [3], the Hall B beamline  
47 is divided into two segments, the so-called “2C” line  
48 from the Beam Switch Yard (BSY) following beam ex-  
49 traction from the CEBAF accelerator to the hall proper,  
50 and the “2H” line from the upstream end of the exper-  
51 imental hall to the beam dump in the downstream tunnel.  
52 The beamline upstream of CLAS12 is furnished with a  
53 number of quadrupoles, corrector dipoles, and beam di-  
54 agnostic tools, grouped into sections. Accelerator op-  
55 erators have exclusive control of these devices and use  
56 this instrumentation to tune and deliver the beam to the  
57 CLAS12 target located approximately at the geometri-  
58 cal center of the hall. In addition to the devices used  
59 by accelerator operations, there are several beam posi-  
60 tion, current, polarization, and halo monitors that are  
61 controlled and monitored by Hall-B shift personnel.

62 For high-energy operation of CLAS12, the 2C beam-  
63 line as described in Ref. [3] was modified to include the  
64 Møller polarimeter located in the upstream tunnel of the  
65 hall and an intermediate beam dump just upstream of  
66 the hall. Additionally, the 2H beamline (Fig. 1) now  
67 includes a cryogenic target and a tungsten shield down-  
68 stream of the target inside the CLAS12 torus magnet  
69 bore. The Møller polarimeter is used to periodically  
70 measure the longitudinal beam polarization and is dis-  
71 cussed in more detail in Sec. 4. The other components  
72 are discussed immediately below.

### 73 2.1. Intermediate beam dump before CLAS12

74 In order to prevent radiation damage to the sensitive  
75 detectors during the initial beam tune, or when errant  
76 beam may be sent to the hall, or during the beam po-  
77 larization measurements with the Møller polarimeter,  
78 the beam has to be terminated upstream of CLAS12.  
79 For these operations the Hall-B tagger dipole magnet is  
80 used to deflect the primary beam and secondary scat-  
81 tering products. During low-energy operations, the tag-  
82 ger dipole directs the beam into the tagger beam dump  
83 in the hall floor upstream of the CLAS12 spectrome-  
84 ter. The highest energy beam that can be directed to this  
85 dump is limited to 6.2 GeV by the maximum field of the  
86 tagger dipole, 1.76 T [4]. At higher energies, a few op-  
87 tions for the intermediate beam dump were considered

88 during the design stage with the optimal solution being  
89 to dump the beam inside the bore of the tagger magnet  
90 yoke. The design of the intermediate dump was based  
91 on full FLUKA [5] simulations and on thermal finite-  
92 element analysis. The two main parameters that were  
93 studied were the radiation levels at the location of the  
94 CLAS12 tracking detectors and the temperature rise in  
95 the magnet yoke when up to 10 nA of continuous wave  
96 (CW) electron beam is dumped on the yoke.

97 The FLUKA simulations were used to determine  
98 background radiation levels at the tracking detectors for  
99 different configurations of the dump and compared with  
100 radiation levels from various targets and beam currents  
101 at the design luminosity. It was found that acceptable  
102 background radiation levels from the dump occur when  
103 the beam is steered into the yoke at approximately 33  
104 cm from the upstream entrance to the tagger magnet  
105 bore, as shown in Fig. 2. This is done by setting the tag-  
106 ger magnetic field to be  $I(A) = 43.491 \times E(\text{GeV}) - 0.076$ ,  
107 where  $I$  and  $E$  are the tagger power supply current and  
108 the beam energy, respectively.

109 The FLUKA simulations were also used to guide the  
110 design of the shielding around and just downstream of  
111 the tagger magnet yoke. The shielding includes lead,  
112 borated polyethylene, and concrete blocks. Figure 3  
113 shows the 1-MeV neutron equivalent fluency for the  
114 background from the dump and for various beam/target  
115 configurations as a function of the position along the  
116 beamline. In the graph, the yoke dump position is at  
117 approximately -900 cm and the CLAS12 target is at  
118  $\sim 400$  cm. The figure shows that at the location of  
119 the CLAS12 target, the designed shielding configura-  
120 tion (green points) results in radiation levels from the  
121 yoke comparable to levels for running on a carbon tar-  
122 get at the full design luminosity.

123 To assess the temperature increase in the yoke, a ther-  
124 mal finite-element analysis was set up using ANSYS  
125 Workbench v18 [6]. A simplified CAD model of the  
126 yoke was imported and modified to include a cylindri-  
127 cal heat load representing the beam. The heating pro-  
128 file from the deposition of 1 kW of power in a cylin-  
129 der of one Moliere radius ( $r = 1.7$  cm) and 10 radi-  
130 ation lengths (17 cm) of iron was calculated. Conser-  
131 vatively, adiabatic boundary conditions were applied to  
132 the outer surfaces of the yoke. The model was solved as  
133 a transient thermal analysis with 100 time points over  
134 3600 seconds. At the dump location, the temperature  
135 was found to initially increase rapidly and then stabili-  
136 zed to a maximum temperature increase of  $\Delta T = 54^\circ\text{C}$   
137 as the heat dissipates throughout the yoke volume (see  
138 Fig. 4). Due to the very large volume and heat capac-  
139 ity of the yoke, the temperature is not expected to rise

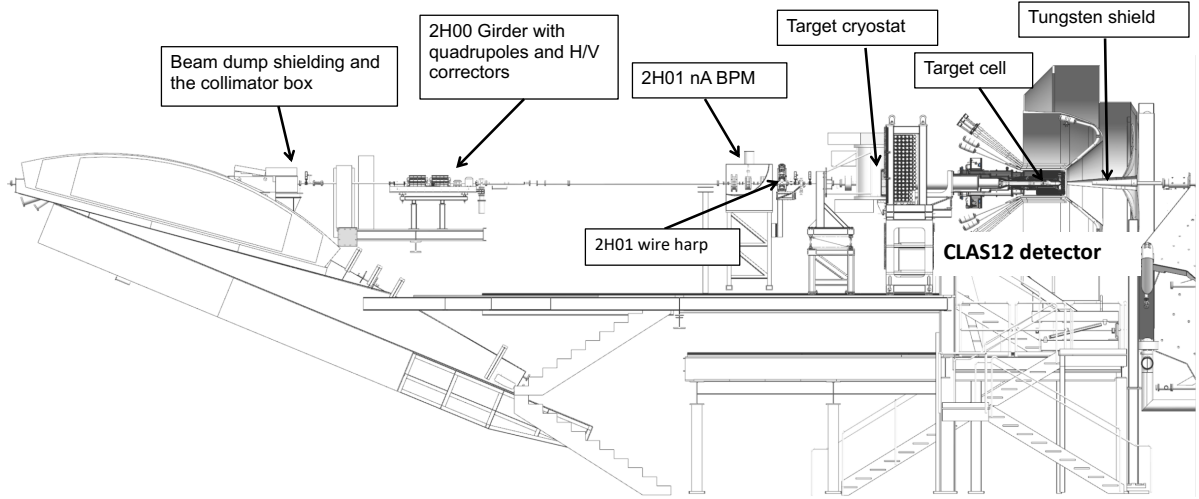


Figure 1: Beamline in Hall B showing beamline elements upstream of the CLAS12 target, cryotarget, CLAS12 central detector and the tungsten shield downstream of the scattering chamber.

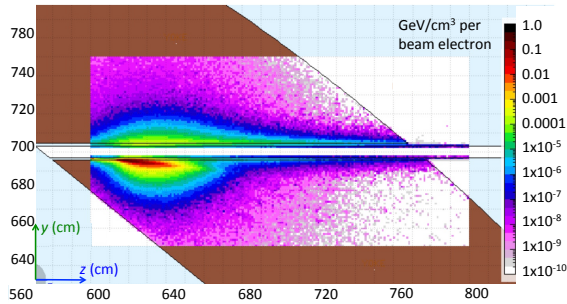


Figure 2: Distribution of energy in the yoke of the tagger dipole magnet from dumping a 10 nA, 11 GeV beam on the yoke at  $\sim 33$  cm from the upstream entrance to the bore of tagger. Horizontal and vertical scales are distances in cm and energy deposition (in  $\text{GeV}/\text{cm}^3$ ) is indicated by the color scale. The brown region indicates the cross section of the tagger yoke.

140 much higher even for longer beam application times.

## 141 2.2. Cryogenic target

142 Hall B experiments are grouped into running periods  
143 according to beam energy and targets. So far two types  
144 of cryogenic targets have been used for experiments;  
145 liquid hydrogen ( $\text{LH}_2$ ) and liquid deuterium ( $\text{LD}_2$ ). The

146 Hall-B cryotarget system from the 6 GeV era [1] has  
147 been modified for CLAS12 operation. The current tar-  
148 get cell is a 20-mm diameter, 50-mm long Kapton cylin-  
149 der with 10-mm-diameter, and 30- $\mu\text{m}$ -thick aluminum  
150 entrance and exit windows. The typical target density is  
151  $71 \text{ mg}/\text{cm}^3$  for  $\text{LH}_2$  and  $169 \text{ mg}/\text{cm}^3$  for  $\text{LD}_2$ . Figure 5  
152 shows the design rendering of the target cell inside the  
153 scattering chamber. The scattering chamber is made of  
154 Rohacell XT110 foam (density  $\rho = 0.110 \text{ g}/\text{cm}^3$ ) and is  
155  $\sim 45$  cm long with a 100 mm outer diameter such that it  
156 fits within the CLAS12 silicon tracker (SVT) (described  
157 elsewhere in this volume) and provides a minimal ma-  
158 terial thickness for scattered particles from the target to  
159 the CLAS12 detectors.

160 A beam halo monitor is integrated within the tar-  
161 get cell. This device consists of a 40-mm-long glass  
162 cylinder with inner and outer diameters of 10 mm  
163 and 12 mm, respectively, mounted directly on the up-  
164 stream window of the target cell with its axis parallel  
165 to the beamline and with 16 optical fibers attached to  
166 the upstream perimeter of the cylinder. Light gener-  
167 ated in the cylinder from interactions of the beam halo  
168 or from back-scattered secondaries are readout with a  
169 multi-anode photomultiplier tube. The device, called  
170 the beam-offset monitor (BOM), is used to monitor the

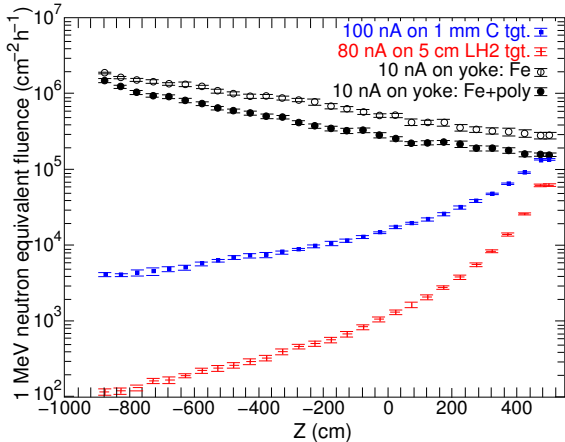


Figure 3: FLUKA simulation of radiation levels in the hall from dumping a 10 nA, 11 GeV beam on the tagger magnet yoke compared to the radiation levels from nominal running on hydrogen and carbon targets.

beam position at the target (see discussion below).

The scattering chamber extends downstream of the Central Detector. There is a 50- $\mu\text{m}$ -thick aluminum window on the downstream end of the scattering chamber that closes the upstream vacuum beamline (from the accelerator to the CLAS12 target). The downstream vacuum beamline starts after a 60-cm-long air gap after the scattering chamber and ends at the beam dump.

In addition to the cryogenic targets mentioned above and already used in two experiments (LH<sub>2</sub> and LD<sub>2</sub>), there will be experiments that will use nuclear targets in the form of thin foils and experiments with polarized targets. The nuclear target assembly is similar to the cryogenic target cell except that various target foils will be inside the cell instead of a liquid. The cryotarget supply lines will be used to flow helium gas through the cell to dissipate heat in the foils from the beam. Two types of polarized targets will be used for CLAS12 experiments [7]; dynamically (longitudinally) polarized ammonia (NH<sub>3</sub>) and deuterated ammonia (ND<sub>3</sub>), and a polarized solid HD target in a frozen spin mode.

### 2.3. Shielding downstream of the target

Special care was taken to protect the CLAS12 detectors from beam-induced background radiation. The main sources of the background are small-angle electron scattering along with electromagnetic processes such as bremsstrahlung, pair production, and Møller scattering. These interactions produce photons, electrons, and positrons that can flood the tracking detectors. GEANT4 simulations of CLAS12 have been used

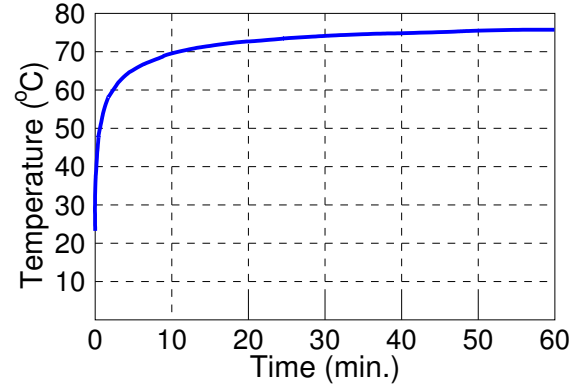


Figure 4: The heat distribution after 60 minutes of beam exposure at the upstream dump location is shown. The highest temperature in the yoke is at the region of the impact and is 76°C assuming an initial uniform temperature of 22°C.

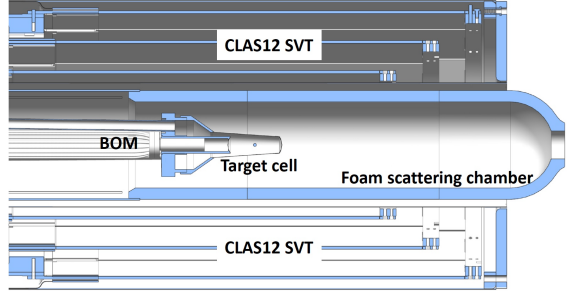


Figure 5: Sketch of the cryogenic target showing the target cell, beam offset monitor, and scattering chamber with associated plumbing and structural supports.

to study backgrounds and design appropriate shielding to reduce the levels of background radiation. The shielding design takes advantage of the 5-T longitudinal magnetic field around the target that is generated by the Central Detector superconducting solenoid magnet. This strong longitudinal magnetic field causes low-energy particles to spiral forward and away from the detectors and into the shielding far downstream of the target. The heavy shielding materials (lead and tungsten) contain the background and either absorb it or guide the flux of particles out the downstream end of CLAS12 without interacting in the detectors.

Because CLAS12 will run with and without the Forward Tagger (FT) (described elsewhere in this volume) in use, two shielding configurations were designed. Figure 6 shows the configuration when the FT is in use. The shielding starts with a tungsten cone with a 5-cm diameter hole at the center for the beam. When the FT is in use, the tungsten cone is mounted directly to the

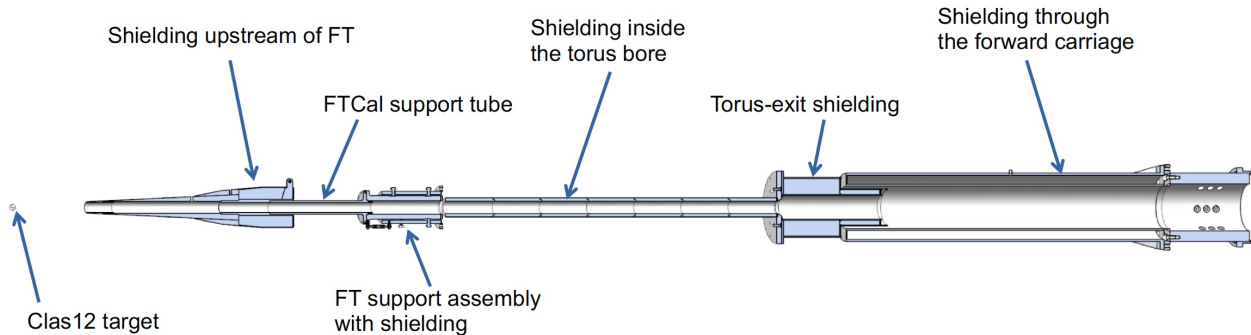


Figure 6: Tungsten shielding downstream of the target, through the torus magnet bore.

220 FT central support, which is also made from tungsten.  
 221 In this case, the angular acceptance of particles scat-  
 222 tered from the target starts at  $\sim 2^\circ$ . For the config-  
 223 uration without the FT, a large diameter lead cylinder is  
 224 inserted between the FT central support (after removing  
 225 the FT tracker) and the tungsten cone, thus moving the  
 226 cone closer to the target. In this case the acceptance for  
 227 forward scattered particles starts at  $\sim 5^\circ$ . The shield-  
 228 ing elements also include cylindrical tungsten absorbers  
 229 inside the torus bore, a tungsten shield around the FT  
 230 mounting fixture to the torus, and a lead-tungsten shield  
 231 downstream of the torus.

One of the main criteria for the shielding design is to maintain an occupancy rate in the drift chambers (described elsewhere in this volume) of less than 4% since higher occupancies adversely affect the track reconstruction efficiency. Drift chamber occupancies were simulated by accumulating hits in the detector elements over 250-ns time frames, which roughly corresponds to the time readout window for the drift chambers. The simulated beam was spread out over this time window to match the actual beam structure and was incident on the 5-cm-long LH<sub>2</sub> target such that the design luminosity of 10<sup>35</sup> cm<sup>-2</sup> s<sup>-1</sup> was achieved in the simulation. The simulated target included the aluminum entrance and exit foils and the air gap downstream of the target. The final shielding configuration resulted in occupancies of less than about 3% for the FT-on configuration and less than about 1.5% for the FT-off configuration. Figure 7 shows the origins of background particles hitting the drift chambers for both shielding configurations. The main source of the background is the target with other sources being the edges of the tungsten shield, and de-

253 tector enclosures (see figure caption for details).

### **3. Beamline Monitoring and Performance**

During a typical experiment, Hall-B shift personnel monitor key beam parameters while beam delivery is controlled by operators in the Machine Control Center. The relevant beamline elements that are used to measure and monitor the key beam parameters are listed in Table 2.

The Synchrotron Light Monitor (SLM) is a photomultiplier tube (PMT) that measures the synchrotron light generated in the last dipole magnet that bends the beam into the Hall-B 2C beamline. The amplitude of the SLM PMT signal is proportional to the beam current and is used to measure the helicity dependence of the beam charge. Due to its dependence on the beam position, it cannot be used as a long term beam current measurement device.

The nano-amp Beam Position Monitors (nA-BPMs) [8] measure the beam current and relative beam position in the transverse, or  $x$ - $y$ , plane ( $z$  is along the beam direction). The beam position in each direction is measured to an absolute accuracy of  $50\ \mu\text{m}$ . The beam current can be measured to an accuracy of  $\sim 1\%$  at beam currents above  $10\ \text{nA}$ , stable over weeks of running. Information from the nA-BPMs can also be used in a feedback loop to keep the beam position fixed.

The wire harps [9] are used to measure the transverse beam profile. These are devices with 25- $\mu\text{m}$  tungsten wires mounted in the horizontal and vertical directions on a support fork that moves the wires into the beam at 45°. As the harp moves into beam, count rates from

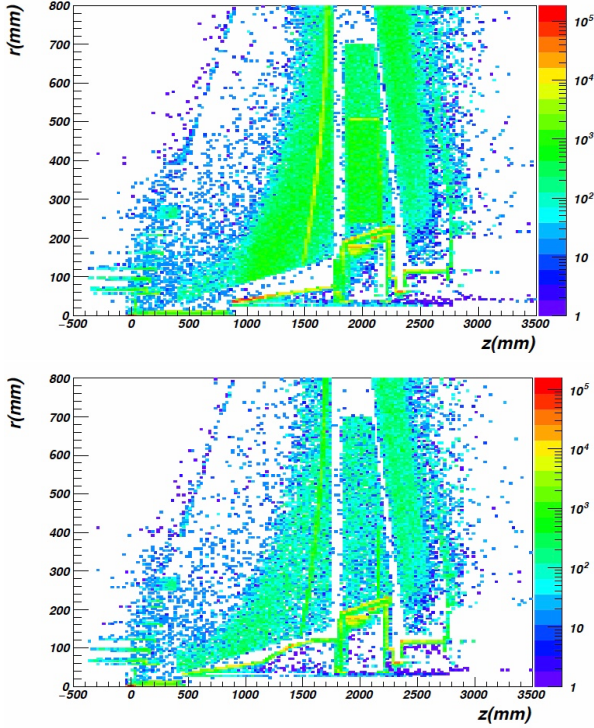


Figure 7: The origin of particles hitting Region 1 drift chambers in the  $R$ - $z$  plane, where  $R$  is the transverse distance from the beam and the  $z$  is in the beam direction. The top graph corresponds to the FT-on configuration and the bottom graph is for FT-off. The main source of the background is the target located at  $R = 0$  and  $z = 0$ . The second largest source is the edge of the tungsten shield that starts from (40,850) and extends to (60,1700), followed by the outer edge of the Forward Tagger calorimeter enclosure located around  $R = 200$  mm and  $z = 2000$  mm. The other large source is the mirror of the high-threshold Cherenkov counter shown as almost vertical band at around  $z = 1550$  mm.

beam halo counters are combined with the wire position information to determine the beam profile. Since this is an invasive measurement, it is performed primarily during beam setup or when other devices indicate a problem with the beam.

The beam halo counters are PMT-based devices located at various positions along the beamline and are mounted very close to the beam; usually strapped directly to the beam pipe. The PMTs have either scintillating or Cherenkov-light-producing plastic mounted on the photocathode. In addition to providing count rates for the wire harps, these counters are sensitive to any beam halo or undesirable beam interactions. These counters are the main tools to monitor beam-induced background in the hall and, along with the BOM, provide feedback signals for the machine fast shutdown

Table 2: Elements of the Hall-B beamline actively monitored and controlled by the experiment shift personnel.

Name and description	Distance from center of the hall (meters)
Synchrotron Light Monitor	-43.
Wire harp 2C21	-38.8
nA-BPM 2C21A	-37.6
Møller polarimeter	-31.5
nA-BPM 2C24A	-24.5
Wire harp 2C24	-22.0
Upstream halo monitors	-21.7
Hall-B tagger dipole	-17.6
Collimator	-15.3
nA-BPM 2H01	-8.0
Wire harp 2H01	-7.4
Midstream halo monitors	-3.9
CLAS12 target	0
Downstream halo monitors	7.5
Beam viewer 2H04	24.0
Dump, Faraday cup	27.0

system (FSD). The FSD will stop beam delivery in the case of excessively high background rates in order to protect the detectors.

Other devices that Hall B uses to monitor and measure beam parameters are the Møller polarimeter located in the upstream tunnel for beam longitudinal polarization measurement, a Faraday cup in the downstream tunnel (electron beam dump) for precise beam current measurement, and a beam viewer that looks at a retractable fluorescent screen installed before the Faraday cup for visual verification of beam transport to the dump.

The Experimental Physics and Industrial Control System (EPICS) [10] is used for monitoring the beam delivery and for control of the beamline devices. Graphical User Interfaces (GUIs) for each application are built using the CS-Studio tools [11]. All variables available in EPICS are archived using the Jefferson Lab MYA data archiver [12]. For continuous monitoring of the beam and the state of the beamline devices, one single GUI was deployed that contains monitored quantities from the beam halo counter rates, magnets, vacuum, cryotarget, beam positions and currents, as well as state of moving devices. For convenience of monitoring, a timeline of counter rates, along with BPM positions and beam current readings can be displayed separately.

Establishing a production quality electron beam for experiments in Hall B is a two-step process. First, the

beam is delivered and tuned in the 2C beamline in the Hall-B upstream tunnel. During this tuning process the beam is dumped on the tagger yoke to protect CLAS12 detectors from excessive radiation exposure. Once the 2C beamline is tuned, the beam is then sent to the downstream electron dump and tuned onto the CLAS12 target. During the tuning process, the beam profile and transverse position are optimized using the information from the wire harps, the nA-BPMs, and the beam halo counters. The beam is accepted for physics production running when all the relevant parameters are within expected limits. After production beam has been established, limits on the halo counter rates, beam position, and beam current are set in the CS-Studio alarm system to help Hall-B shift personnel to monitor the beam quality when running experiments.

### 3.1. Beam profile and position stability

Establishing and maintaining a high-quality beam is important for obtaining high-quality physics data. Once the beam has been established, scans using the wire harps and nA-BPMs are stored in the MYA archive and are used as reference values over the course of an experimental running period. Figure 8 shows the  $x$ - and  $y$ -profiles measured with wire harps 2C21 and 2H01, located in the upstream tunnel of Hall B and at 7.4 m upstream of the target, respectively. During these measurements, the beam was delivered to the Faraday cup. Figure 9 shows a histogram of the  $x$ - and  $y$ -widths for sixteen 2H01 harp scans taken over a two month running period. The beam width in both directions fluctuates between 180  $\mu\text{m}$  to 300  $\mu\text{m}$  with an average value of 250  $\mu\text{m}$ .

After the beam has been established for physics running, its position and current stability are continuously monitored using the halo counter rates and the nA-BPMs. Figure 10 shows the distribution of the  $x$ - and  $y$ -positions about the mean at the 2H01 nA-BPM. The RMS of both distributions is on order of 20  $\mu\text{m}$ . Such stability is largely due to use of the beam orbit lock system that uses the position readings of nA-BPMs to drive horizontal and vertical correctors that keep the position of the beam at the set points established at the start of a running period.

### 3.2. Beam charge measurement

An accurate measurement of the total amount of beam charge incident on the target during an experiment is vital for the measurement of experimental cross sections. The Hall-B Faraday cup (FC) is the main tool to obtain an accurate *absolute* beam current measurement. A description of the Faraday cup and its readout

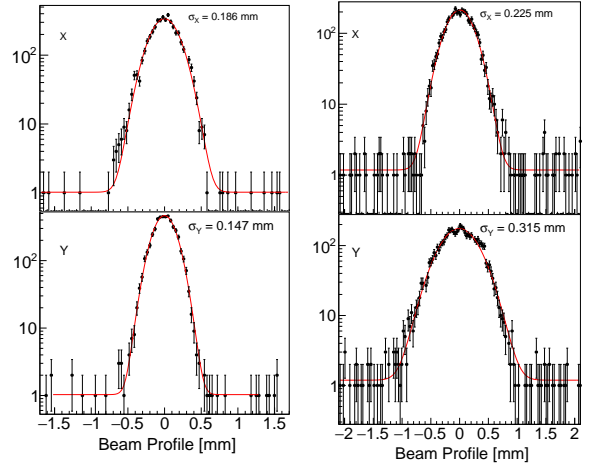


Figure 8: Beam  $x$ - (top) and  $y$ -profiles (bottom) measured using the wire harp scanners at 2C21 (left) and at 2H01 (right). The red curve is a Gaussian fit with the width shown by the  $\sigma$  values.

electronics can be found in Ref. [1]. Since the Faraday cup does not have active cooling, it is limited to 175 W of beam power for long exposures. However, most of the CLAS12 experiments will run with beam currents that exceed the power limit of the FC, thus requiring another method of measuring the beam current. The other devices used to monitor the beam current during the experiment are the nA-BPMs and the SLM, but these devices do not have the long-term stability to provide the accuracy needed over the weeks-long course of an experiment.<sup>1</sup>

Instead, a 5-kW beam dump can be inserted in front of the FC during high-power running. This insertable dump, or beam blocker, is a water-cooled, 28-cm-long copper cylinder (19.5 radiation lengths). While most of the beam is deposited in this beam blocker, the FC still measures a leak-through current that is proportional to the total beam current with a very high accuracy of better than 0.5%. In order to use the FC current measurement with the blocker in, a beam-current attenuation factor,  $A$ , must be determined for every beam energy, so that the beam current is given by  $I = AI_{FC}^{in}$ , where  $I_{FC}^{in}$  is the beam current measured at the FC when the beam blocker is in.

To calibrate the attenuation factor, first, a scan of the beam current up to the highest current required by the experiment is done without the beam blocker. The scan is quick so as to not overheat the FC. These data are used

<sup>1</sup>The calibration of the nA-BPMs relative to the FC remains stable within a few % for a period of time sufficient for coarse monitoring of the beam current during the experiment.

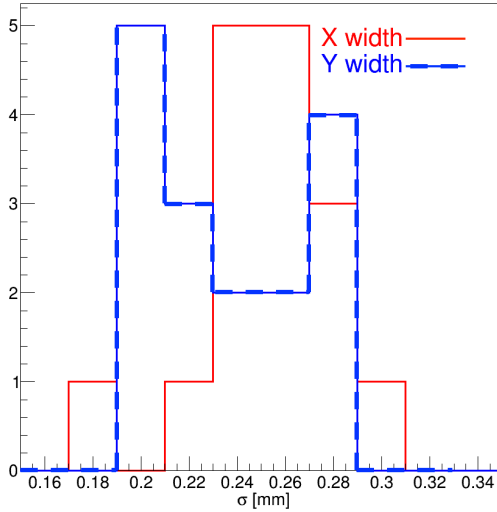


Figure 9: Beam width measured with the 2H01 wire harp over two months of running. The  $x$ -width is shown in solid red and the  $y$ -width is shown in dashed blue.

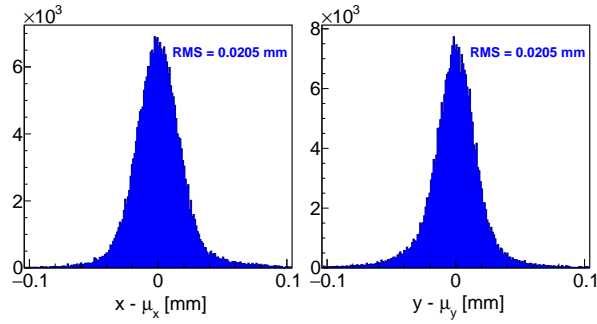


Figure 10: Beam position deviations,  $x - \mu_x$  (left) and  $\mu_y$  (right), over a month of running as measured by the 2H01 nA-BPM.

to calibrate the nA-BPM current readings relative to the FC with a calibration factor given by  $C = I_{BPM}/I_{FC}$ , where  $I_{BPM}$  and  $I_{FC}$  are the currents measured by the nA-BPM and FC, respectively. The left panel of Fig. 11 shows a distribution of  $C$  for a range of beam currents from 15 to 80 nA at a beam energy of 10.67 GeV using the 2C21 nA-BPM. The distribution has a mean of  $\langle C \rangle = 1.057$  and Gaussian width of  $\sigma_C = 0.0038$ , which we use to determine the relative uncertainty in the calibration factor of  $\delta C/C = \sigma_C/\langle C \rangle = 0.36\%$ .

In the second step, a similar current scan is performed but with the insertable beam blocker in place. Using the now calibrated values of the nA-BPM current reading from the first step, the attenuation factor is given by  $A = I_{BPM}^{in}/I_{FC}^{in}$ . The distribution of  $A$  is shown in the right panel of Fig. 11, which has also been obtained for

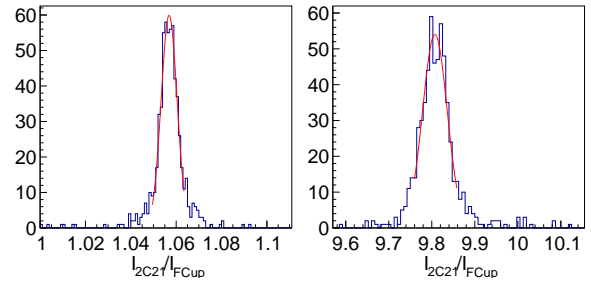


Figure 11: The ratio of beam currents measured by the 2C21 nA-BPM and the Faraday cup without (left) and with (right) the insertable beam blocker. Each distribution has been fit with a Gaussian to obtain the means and widths given in the text.

a range of beam currents from 15 to 80 nA at a beam energy of 10.67 GeV using the 2C21 nA-BPM. The distribution has a mean of  $\langle A \rangle = 9.807$  and a Gaussian width of  $\sigma_A = 0.0306$ , which leads to a relative uncertainty of  $\delta A/A = \sigma_A/\langle A \rangle = 0.31\%$ . Combining the uncertainties from the calibration of the nA-BPMs and the attenuation factor leads to a total relative uncertainty in the blocker-in FC current measurement of  $\delta I_{FC}/I = 0.48\%$ .

A simultaneous measurement of the attenuation factor has been done using the 2C24 nA-BPM resulting in  $\langle A \rangle = 9.809$ , which agrees well with the 2C21 nA-BPM measurement. More details of this calibration can be found in Ref. [13]. Results obtained for other energies are shown in Table 3 with details found in Ref. [14].

Beam energy (GeV)	FC Attenuation
6.4	16.28
6.6	16.24
7.54	14.90
10.2	9.96
10.67	9.81

Table 3: FC attenuation factors for different beam energies. The estimated relative uncertainty of the attenuation factor is < 0.5%.

#### 4. Møller Polarimeter

Determination of the electron beam polarization is done in Hall B using a coincidence Møller polarimeter. The polarimeter is based on  $\vec{e} + \vec{e} \rightarrow e + e$  elastic scattering (Møller scattering). A detailed description of Møller scattering is presented in Ref. [15].

For a longitudinally polarized electron beam incident on a longitudinally polarized electron target, the center-of-momentum (CM) frame cross section is given by [16,

$$446 \quad \frac{d\sigma}{d\Omega} = \frac{d\sigma_0}{d\Omega} (1 + P_B A_{zz} P_T), \quad (1)$$

447 where  $d\sigma_0/d\Omega$  is the unpolarized cross section,  $P_B$  and  
 448  $P_T$  are the longitudinal components of the beam and  
 449 target polarization, respectively, and  $A_{zz}$  is the analyzing  
 450 power. The unpolarized cross section and analyzing  
 451 power can be precisely calculated through QED, which  
 452 gives

$$453 \quad \frac{d\sigma_0}{d\Omega} = \left( \frac{\alpha (3 + \cos^2 \theta_{CM})}{2m_e \gamma \sin^2 \theta_{cm}} \right)^2, \quad (2)$$

454 and

$$455 \quad A_{zz} = -\frac{(7 + \cos \theta_{CM}) \sin^2 \theta_{CM}}{(3 + \cos^2 \theta_{CM})^2}, \quad (3)$$

456 where  $\alpha$  is the fine structure constant,  $\theta_{CM}$  is the center  
 457 of momentum scattering angle,  $m_e$  is the electron mass,  
 458 and  $\gamma = \sqrt{(E + m_e)/2m_e}$  with  $E$  the lab energy of the  
 459 incident electron. From the above formulas, one sees  
 460 that  $A_{zz}$  has a maximum magnitude of 7/9 at  $\theta_{CM} = 90^\circ$ ,  
 461 which is the central scattering angle for our polarimeter.

462 Forming the beam-helicity-dependent asymmetry  
 463 gives

$$464 \quad A = \frac{\frac{d\sigma}{d\Omega_+} - \frac{d\sigma}{d\Omega_-}}{\frac{d\sigma}{d\Omega_+} + \frac{d\sigma}{d\Omega_-}} = A_{zz}(\theta_{CM}) P_B^z P_T^z, \quad (4)$$

465 where the  $\pm$  refers to cases where the beam helicity and  
 466 the target polarization are aligned or anti-aligned. The  
 467 asymmetry can be measured from the yields according  
 468 to

$$469 \quad A = \frac{N_+ - N_-}{N_+ + N_-} = \langle A_{zz} \rangle P_B^z P_T^z, \quad (5)$$

470 where  $\langle A_{zz} \rangle$  is the effective analyzing power corrected  
 471 for the finite-angle acceptance of the polarimeter and  
 472 atomic-electron motion (also known as the Levchuk ef-  
 473 fect [18]).

474 The CLAS12 Møller polarimeter detects the scattered  
 475 electrons in coincidence near  $\theta_{CM} = 90^\circ$ , the peak of  
 476  $A_{zz}$ . The coincidence method has the advantage, as com-  
 477 pared to single-arm Møller polarimetry, of producing a  
 478 clean data set without having to do energy-dependent  
 479 background subtractions (see, for example Ref. [19]).  
 480 Accidental background rates are typically less than 10%  
 481 of the real coincident rate for our polarimeter. The acci-  
 482 dental rate is measured and included as a correction.

#### 483 4.1. Polarimeter Design

484 The layout for the polarimeter is shown in Fig. 12.  
 485 The essential elements of the polarimeter include a po-  
 486 larized target system, a pair of quadrupole magnets both  
 487 operated in a dispersive mode to separate the scattered  
 488 electrons from the unscattered beam electrons, a pair  
 489 of detectors, and lead shielding between the second  
 490 quadrupole and the detectors to reduce background. The  
 491 detectors consist of scintillating fibers packed with lead  
 492 powder to form a 15.6-cm wide, 9.0-cm high, and 25-  
 493 cm deep block with a light guide and are read out with a  
 494 PMT. The detectors are surrounded by lead bricks with  
 495 a scattered-particle aperture of 7.62 cm in the hori-  
 496 zontal direction and 5.0 cm in the vertical direction. The  
 497 locations of the quadrupoles and detectors along with  
 498 the quadrupole fields were determined by simulations  
 499 of the layout. The locations and fields were adjusted in  
 500 the simulation so that  $\theta_{CM} = 90^\circ \pm (4^\circ - 4.5^\circ)$ .

##### 4.1.1. Polarimeter Target

501 The target system has a pair of 25-μm-thick permendur  
 502 foils on a remotely controlled insertion table housed  
 503 in a vacuum chamber, as shown in Fig. 13. Permendur  
 504 is an iron-cobalt alloy (49% Fe, 49% Co, 2% Va) that  
 505 has a saturated polarization of approximately 8% along  
 506 the plane of the foil when subjected to a magnetic field  
 507 of greater than about 40 G. To create a longitudinally  
 508 polarized target, the plane of a foil is oriented at  $\pm 20^\circ$   
 509 relative to the beamline and subjected to a longitudinal  
 510 magnetic holding field produced by a pair of Helmholtz  
 511 coils on either side of the target chamber. Since only the  
 512 longitudinal component of the polarization contributes  
 513 to the measured asymmetry, the target polarization used  
 514 in Eq. 5 is  $P_T^z = P_T \cos 20^\circ$ .

515 The polarization of the permendur target is related to  
 516 the magnetization,  $M$ , of the foil by [20]

$$517 \quad P_T = M (4.546 \times 10^{-5} \pm 2.9 \times 10^{-7}), \quad (6)$$

518 where  $M$  is measured in units of G. The foil magnetiza-  
 519 tion is measured in a separate setup consisting of a  
 520 solenoid coil used to produce the magnetizing field,  $H$ ,  
 521 into which the target foil is placed and a pickup coil that  
 522 is located at the center of the foil. A fixed current is ap-  
 523 plied to the solenoid to polarize the target. The direction  
 524 of the current is then flipped over a time period of 0.15  
 525 s leading to an induced voltage across the pickup coil.  
 526 A typical pickup-coil signal is shown in Fig. 14, which  
 527 was measured with a digital storage oscilloscope. The  
 528 flat part of this signal (highlighted by the black constant  
 529 fit) corresponds to the changing applied field while the  
 530 narrow peak in the middle of the signal results from the  
 531

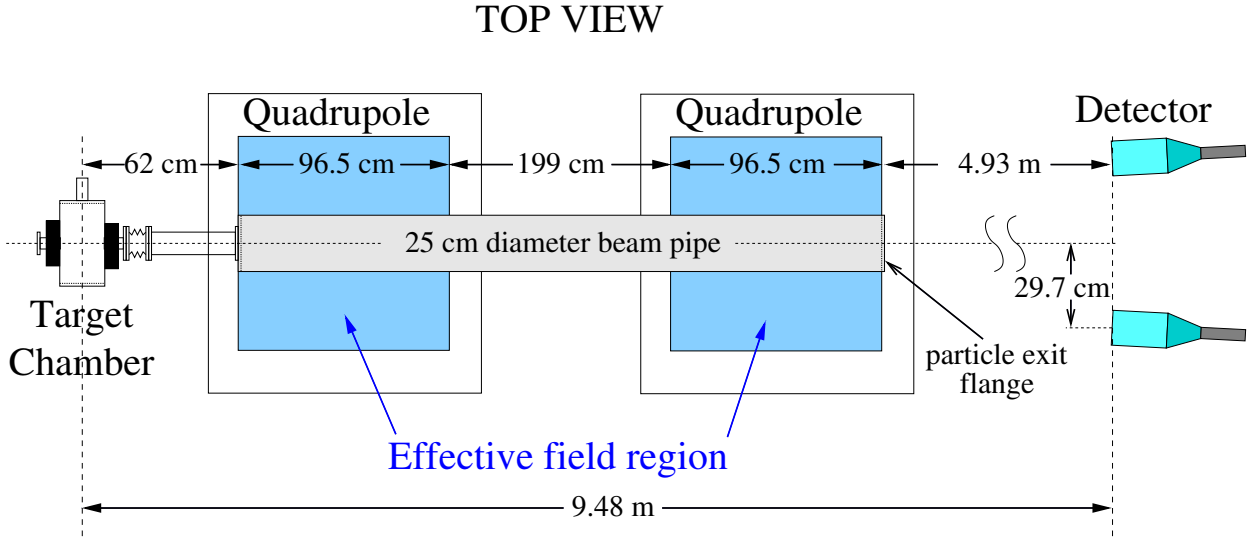


Figure 12: Layout of the CLAS12 Møller polarimeter. Detector shielding is not shown.

532 change in the target foil magnetization. Applying Faraday's law to the flat part of the signal (using the fit to  
 533 interpolate under the peak) yields

$$535 \int_H Vdt = 2HN_T \langle A_{coil} \rangle \rightarrow H = \frac{\int_H Vdt}{2N_T \langle A_{coil} \rangle}, \quad (7)$$

536 where  $\int_H Vdt$  is the area under the pickup coil signal  
 537 excluding the peak,  $N_T$  is the number of turns in the  
 538 pickup coil, and  $\langle A_{coil} \rangle$  is the average cross-sectional  
 539 area of the pickup coil. Since the magnetization is  
 540 related to the total field,  $B$ , and the applied field,  $H$ ,  
 541 through  $4\pi M = B - H$ , then

$$542 M = B - H = \frac{1}{4\pi} H \left( \frac{\int_{\text{total}} Vdt - \int_H Vdt}{\int_H Vdt} \right), \quad (8)$$

543 where  $\int_{\text{total}} Vdt$  is the total area of the signal. Figure 544 shows a typical saturation curve for the target, i.e. how the target polarization depends on the applied field. Measurements were done with two different pickup coils with the difference between the two results indicating the systematic uncertainty associated with knowledge of the coil geometry. For this foil, the polarization saturates at a value of  $7.31 \pm 0.08\%$ , where the uncertainty is a combination of the statistical uncertainties from the linear fits of the saturation region of the curves and the variation between the two measurements. Additional uncertainties associated with converting from  $M$  to  $P_T$  (Eq. 6), the uncertainty from estimated variations in the target material thickness, and the uncertainty in the target angle relative to the beam lead

558 to an overall uncertainty of 0.13% and a total relative  
 559 uncertainty  $\delta P_T^z / P_T^z = 0.018$ .

#### 560 4.2. Analyzing Power Corrections and Uncertainties

561 Simulations have been performed to estimate effects  
 562 due to atomic motion of the electrons and to estimate  
 563 uncertainties associated with the polarimeter geometry.  
 564 The simulation begins by randomly selecting scattering  
 565 angles  $\theta_{CM}$  and  $\phi_{CM}$  and then transports the scattered  
 566 electrons through the magnets and towards the detectors.  
 567 For events in which both electrons hit the detectors we  
 568 determine an average analyzing power,  $\langle A_{zz} \rangle$ .  
 569 The motion of the atomic electrons has been included in  
 570 the simulation according to Ref. [18]. Figure 16 shows  
 571  $\langle A_{zz} \rangle$  as a function of beam energy both with (orange)  
 572 and without (blue) atomic-electron motion included in  
 573 the simulation. The green curve is a fit to the points  
 574  $\langle A_{zz} \rangle = -0.777123 + (2.9249 \times 10^{-3})/E$ . The estimated  
 575 relative uncertainty is < 0.01% and was determined by  
 576 looking at variations in  $\langle A_{zz} \rangle$  for reasonable variations in  
 577 the geometry (locations of quadrupoles and detectors)  
 578 and magnetic fields.

#### 579 4.3. Beam polarization measurements

580 Beam polarization measurements are usually done on  
 581 a weekly basis or after changes to the accelerator con-  
 582 figuration. The shift personnel use what is in essence  
 583 a push-button GUI interface. The user selects which  
 584 target to use (left or right) and the Helmholtz coil po-  
 585 larity. The settings for the quadrupoles are automati-

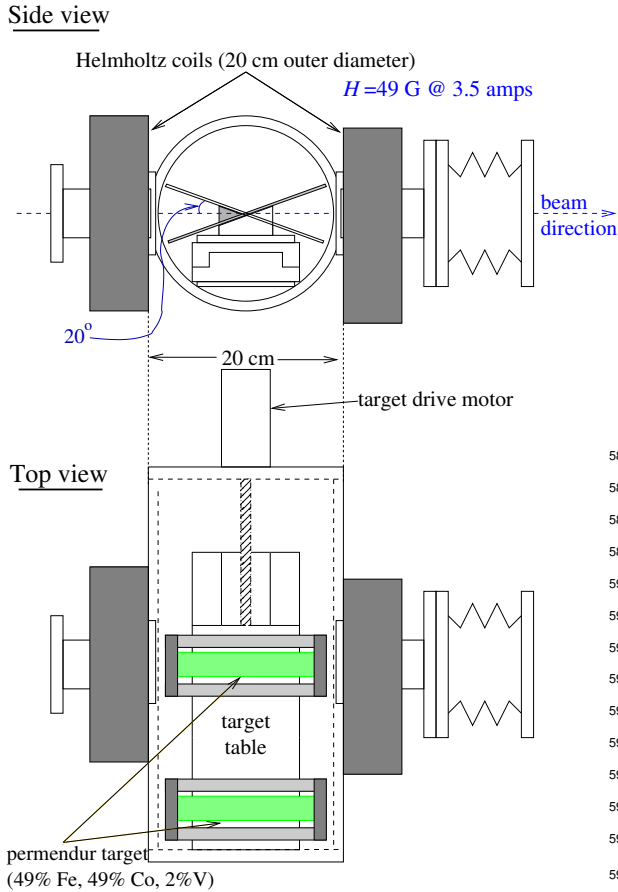


Figure 13: Layout of the CLAS12 Møller polarimeter target chamber. Shown with the beam-left target inserted.

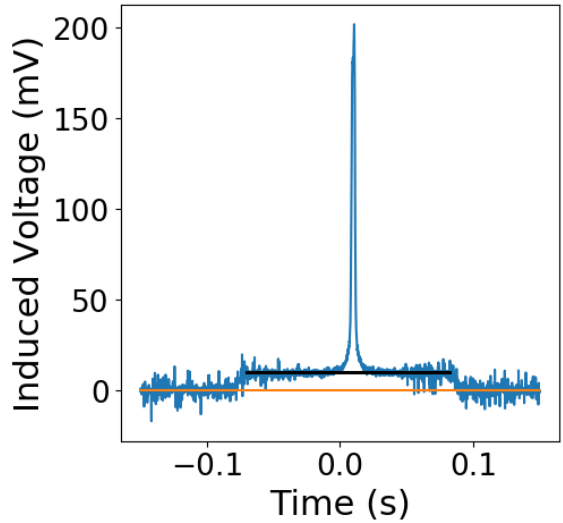


Figure 14: Target pickup coil signal showing induced voltage as a function of time. The flat part of the signal (fit with black line) corresponds to the changing applied Helmholtz field,  $H$ , while the sharp peak near the middle corresponds to the flip in the target magnetization.

586      ically calculated based upon the beam energy. Individual Møller runs are usually done for both targets  
 587      588 with a statistical precision of  $\pm 1.5\%$ , which is slightly smaller than the total systematic uncertainty. The underly-  
 589      590 ing software calculates the beam polarization using the beam-helicity-gated true and accidental coincidence  
 591      592 rates from the Møller detectors along with the beam-  
 593      594 helicity related charge asymmetry measured using the SLM. At the end of a Møller run the beam polarization  
 595      596 is stored in the GUI and goes automatically to the elec-  
 597      598 tronic logbook. The scaler readouts during the run are stored in the run file while polarization the measurement  
 599      600 is stored the database.

601      Results of beam polarization measurements taken  
 602      603 during the fall 2018 run period are shown in Fig. 17.  
 604      There are two distinct regions of beam polarization  
 605      606 with average polarizations of  $85.95\% \pm 1.29\%$  and  
 607      608  $89.22\% \pm 2.51\%$ . These two regions differ by set-  
 609      610 ings of the angle,  $\theta_W$  of the Wien filter in the injector.  
 611      The initial Wien-filter angle was set to maximize the  
 612      613 beam polarization in Hall B and was based on a calcu-  
 614      lation of the electron spin precession in the acceler-  
 615      616 ator. However, the polarization in the early part of the run-  
 617      618 ning period fell below the expected maximum of about  
 619      620 90%, which was measured at the injector by a Mott pol-  
 621      622 arimeter, indicating an incorrectly calculated  $\theta_W$ . In  
 623      624 order to find the optimum value of  $\theta_W$ , two more Møller  
 625      626 measurements of the beam polarization in Hall-B were

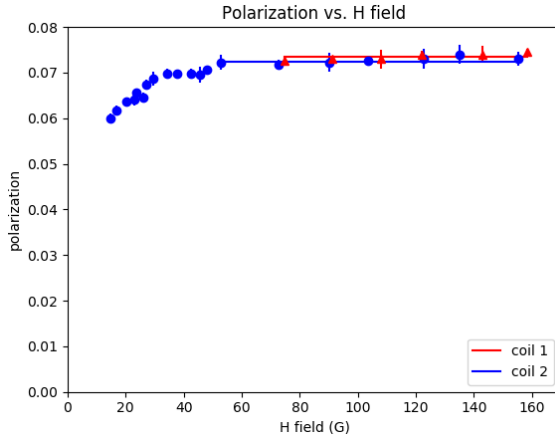


Figure 15: Target polarization vs. applied magnetic field,  $H$ , measured with two different pickup coils. A constant fit to the flat part of the curves yields values of  $7.35 \pm 0.04\%$  for coil 1 (red diamonds) and  $7.24 \pm 0.05\%$  for coil 2 (blue dots).

614 performed at  $\theta_W = 25^\circ$  and  $70^\circ$ . The result of these  
 615 measurements along with the average at  $\theta_W = 50^\circ$  are  
 616 shown in Fig. 18. Fitting these three points with a function of  $a \cos(\theta_W - b)$  (dashed curve), where  $a$  and  $b$  are  
 617 fit parameters, shows that the maximum polarization of  
 618 about 90% in Hall B occurs for  $\theta_W \approx 40^\circ$ .  
 619

620 Figure 17 has two sets of Hall-B polarimeter mea-  
 621 surements done with and without a half-wave plate. The  
 622 half-wave plate rotates the electron spin by  $180^\circ$ . The  
 623 measurements with and without the the half-wave plate  
 624 agree within statistical uncertainties.

## 625 5. Summary

626 The first CLAS12 experiment took data successfully  
 627 at three beam energies; 10.6 GeV, 6.4 GeV and 2.3 GeV  
 628 with a liquid-hydrogen target. High quality beam was  
 629 delivered with a beam size of  $< 200 \mu\text{m}$  and a beam halo  
 630 as small as  $10^{-4}$  at  $5\sigma$  away from the core. The beam  
 631 position was maintained within  $\sim 200 \mu\text{m}$  throughout  
 632 the run by the beam feedback system and the fast shut  
 633 down system worked in protecting the CLAS12 detec-  
 634 tors sensors from errant beam exposure. With typical  
 635 Møller polarimeter runs, the beam polarization can be  
 636 measured to an absolute precision of  $\sim 2.5\%$ .

## 637 6. Acknowledgements

638 The authors are grateful for the outstanding efforts  
 639 by the staff of the Accelerator Division and the Hall B  
 640 Engineering Group at Jefferson Lab during the instal-  
 641 lation and running of the experiment. We also thank

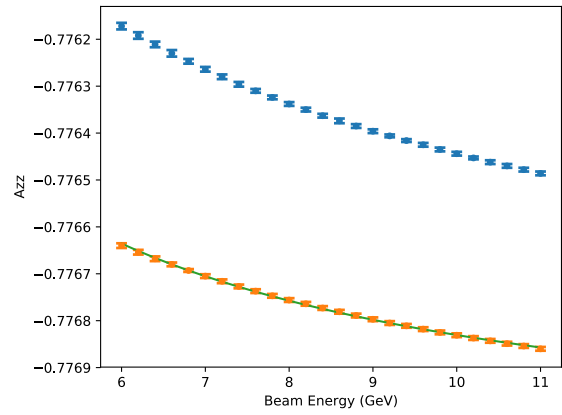


Figure 16: Average analyzing power  $\langle A_{zz} \rangle$  as a function of beam energy from simulation. The orange/blue points include/exclude motion of the atomic electrons. The error bars are statistical only. The green curve on the orange points is a fit given in the text.

642 the CLAS12 collaboration for manning shifts and tak-  
 643 ing high quality data. This material is based upon work  
 644 supported by the U.S. Department of Energy, Office of  
 645 Science, Office of Nuclear Physics under contract DE-  
 646 AC05-06OR23177.

- 647 [1] B. A. Mecking, et al., The CEBAF Large Acceptance Spec-  
   648 trometer (CLAS), Nucl. Instrum. Meth. A503 (2003) 513–553.  
   649 doi:10.1016/S0168-9002(03)01001-5.
- 650 [2] HPS update to PAC39, [https://www.jlab.org/exp\\_prog/proposals/12/C12-11-006.pdf](https://www.jlab.org/exp_prog/proposals/12/C12-11-006.pdf).
- 651 [3] N. Baltzell, et al., The Heavy Photon Search beamline and its  
   652 performance, Nucl. Instrum. Meth. A859 (2017) 69–75. [arXiv:1612.07821](https://arxiv.org/abs/1612.07821), doi:10.1016/j.nima.2017.03.061.
- 653 [4] D. I. Sober, et al., The bremsstrahlung tagged photon beam in  
   654 Hall B at JLab, Nucl. Instrum. Meth. A440 (2000) 263–284.  
   655 doi:10.1016/S0168-9002(99)00784-6.
- 656 [5] T. T. Bohlen, F. Cerutti, M. P. W. Chin, A. Fassò, A. Ferrari, P. G.  
   657 Ortega, A. Mairani, P. R. Sala, G. Smirnov, V. Vlachoudis, The  
   658 FLUKA Code: Developments and Challenges for High Energy  
   659 and Medical Applications, Nucl. Data Sheets 120 (2014) 211–  
   660 214. doi:10.1016/j.nds.2014.07.049.
- 661 [6] <https://www.ansys.com/-/media/Ansystech/corporate/resourcecenter/brochure/ansyscapabilities180.pdf>.
- 662 [7] C. Keith, Polarized Solid Targets at Jefferson Lab, PoS  
   663 PSTP2015 (2015) 013. doi:10.22323/1.243.0013.
- 664 [8] R. Ursic, M. Piller, R. Flood, E. Strong, L. Burlinton, 1 nA  
   665 Beam Position Monitoring System, Conf. Proc. C970512 (1997)  
   666 2131.
- 667 [9] M. McCaughan, M. Tiefenback, D. Turner, Improvements to  
   668 Existing Jefferson Lab Wire Scanners, in: Proceedings, 4th  
   669 International Particle Accelerator Conference (IPAC 2013):  
   670 Shanghai, China, May 12–17, 2013, 2013, p. MOPWA076.  
   671 URL <http://JACoW.org/IPAC2013/papers/mopwa076.pdf>
- 672 [10] <https://epics-controls.org>.
- 673 [11] <http://controlsystemstudio.org>.
- 674 [12] C. Slominski, [https://wiki.jlab.org/lerf/images/7/75/Archive\\_user.pdf](https://wiki.jlab.org/lerf/images/7/75/Archive_user.pdf).
- 675 [13] R. Paremuzyan, S. Stepanyan, CLAS12 Note 2018-003 (2018).

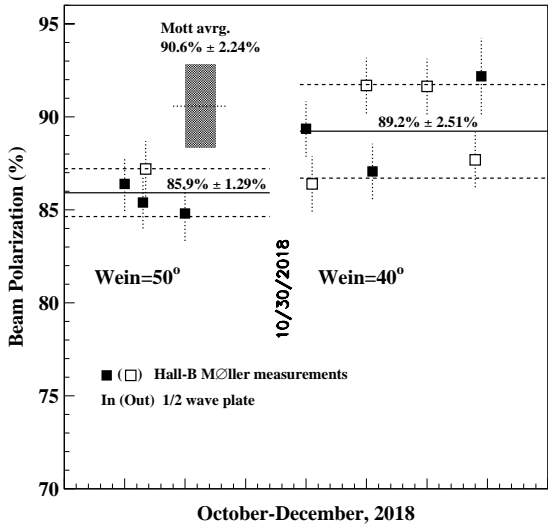


Figure 17: Beam polarization measured in Hall B during the fall 2018 running period. Prior to October 30 the measurements from the Hall-B polarimeter (squares) averaged to  $85.9\% \pm 1.2\%$  (stat.), which is lower than the expected 90% from the injector Mott measurements (black band). After optimizing the Wien-filter angle the average polarization measured in Hall B was measured to be  $89.2\% \pm 2.5\%$  (stat.). Filled and open symbols correspond to measurements made with and without a half-wave plate, respectively. Error bars are statistical only.

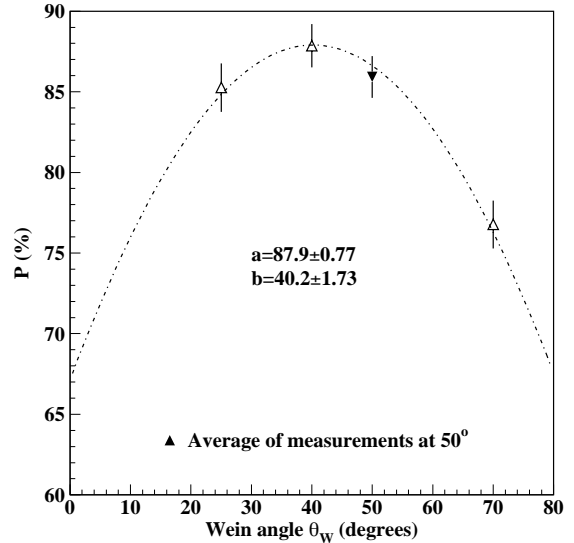


Figure 18: Beam polarization measurements at different Wien angle settings taken during the fall 2018 run period. The dashed curve is the cosine-function fit to the data points. The filled point is the average over all measurements with the angle set to  $50^\circ$  and the open points are from single measurements. Error bars are statistical only.

709

00984-4.

- 681 [link].  
682 URL <https://misportal.jlab.org/mis/physics/clas12/viewFile.cfm/2018-004.pdf?documentId=58>  
683  
684 [14] R. Paremuyan, S. Stepanyan, CLAS12 Note 2018-004 (2018).  
685 [link].  
686 URL <https://misportal.jlab.org/mis/physics/clas12/viewFile.cfm/2018-003.7gev.pdf?documentId=57>  
687  
688 [15] B. Wagner, H. G. Andresen, K. H. Steffens, W. Hartmann,  
689 W. Heil, E. Reichert, A Moller polarimeter for CW and pulsed  
690 intermediate-energy electron beams, Nucl. Instrum. Meth. A294  
691 (1990) 541–548. doi:10.1016/0168-9002(90)90296-I.  
692  
693 [16] C. Møller, Ann. Phys. 14 (1932) 531.  
694 [17] A. A. Kresnin, L. N. Rosentsveig, J. Exp. Theor. Phys. (USSR)  
695 32 (1957) 353.  
696 [18] L. G. Levchuk, The Intraatomic motion of bound electrons  
697 as a possible source of a systematic error in electron beam  
698 polarization measurements by means of a Moller polarimeter,  
699 Nucl. Instrum. Meth. A345 (1994) 496–499. doi:10.1016/0168-9002(94)90505-3.  
700  
701 [19] J. Arrington, E. J. Beise, B. W. Filippone, T. G. O'Neill, W. R.  
702 Dodge, G. W. Dodson, K. A. Dow, J. D. Zumbro, A Variable  
703 energy Moller polarimeter at the MIT-Bates Linear Accelerator  
704 Center, Nucl. Instrum. Meth. A311 (1992) 39–48. doi:10.1016/0168-9002(92)90849-Y.  
705  
706 [20] H. R. Band, G. Mitchell, R. Prepost, T. Wright, A Moller  
707 polarimeter for high-energy electron beams, Nucl. Instrum.  
708 Meth. A400 (1997) 24–33. doi:10.1016/S0168-9002(97)